research papers

CrossMark

Image guidance protocol for synchrotron microbeam radiation therapy

Daniele Pelliccia,[a,b]* Christopher M. Poole,[a] Jayde Livingstone,[b] Andrew W. Stevenson,[b,c] Lloyd M. L. Smyth,[d] Peter A. W. Rogers,[d] Daniel Haüsermann[b] and Jeffrey C. Crosbie[a]

[a]School of Science, RMIT University, Melbourne, Victoria 3001, Australia, [b]Australian Synchrotron, Clayton, Victoria 3168, Australia, [c]CSIRO, Clayton, Victoria 3168, Australia, and [d]The University of Melbourne, Department of Obstetrics and Gynaecology, The Royal Women's Hospital, Parkville, Victoria 3052, Australia. *Correspondence e-mail: daniele.pelliccia@rmit.edu.au

The protocol for image-guided microbeam radiotherapy (MRT) developed for the Australian Synchrotron's Imaging and Medical Beamline (IMBL) is described. The protocol has been designed for the small-animal MRT station of IMBL to enable future preclinical trials on rodents. The image guidance procedure allows for low-dose monochromatic imaging at 50 keV and subsequent semi-automated sample alignment in 3D with sub-100 μm accuracy. Following the alignment, a beamline operation mode change is performed and the relevant beamline components are automatically aligned for the treatment (pink) beam to be delivered on the sample. Here, the small-animal MRT station, the parameters and procedures for the image guidance protocol, as well as the experimental imaging results using phantoms are described. Furthermore, the experimental validation of the protocol using 3D PRESAGE® dosimeters is reported. It is demonstrated that the sample alignment is maintained after the mode change and the treatment can be delivered within the same spatial accuracy of 100 μm. The results indicate that the proposed approach is viable for preclinical trials of small-animal MRT.

1. Introduction

Microbeam radiation therapy (MRT), using X-rays generated by a synchrotron facility (Slatkin *et al.*, 1992, 1995; Laissue *et al.*, 1999), is a novel preclinical form of radiotherapy that shows promise of providing a major advance in cancer control if successfully translated to clinical practice (Laissue *et al.*, 1998; Dilmanian *et al.*, 2002; Bräuer-Krisch *et al.*, 2010; Grotzer *et al.*, 2015).

To generate MRT, the synchrotron beam (mean energy of about 100 keV) is segmented by a collimator into a lattice of micro-planar beams, usually 25–50 μm wide (see, for example, Bräuer-Krisch *et al.*, 2010), spaced at regular intervals of 200–400 μm, with minimal divergence. Typical radiation doses are 300–1000 Gy along the microbeam path (peak dose), and 5–20 Gy in the valleys between the beams. Peak dose values are a few orders of magnitude larger than the average dose values delivered in conventional radiotherapy; the spatial fractionation and the limited divergence of the beam, however, facilitates normal tissue recovery while, at the same time, destroying tumor cells (Crosbie *et al.*, 2010).

The purpose of image guidance in clinical radiotherapy is to guarantee precise control of the radiation field to accurately deliver the prescribed dose to the target and not its surroundings (Timmerman & Xing, 2012). In the case of

synchrotron MRT, a valid protocol must be able to generate real-time images of the patient and register these with radiological images from a treatment plan developed for the patient prior to arrival at the synchrotron. Data obtained with image guidance will inform decisions about patient positioning.

In synchrotron MRT, the imaging and treatment beams come from the same source but cannot be used at the same time. Therefore the image guidance procedure must ensure that the change from imaging beam to therapy beam is achieved with high spatial accuracy and in a short time-frame. The latter is a crucial requirement for image-guided MRT of small animals like rodents, which should be kept under anaesthesia for as short a time as feasibly possible.

An image guidance modality based on a modification of the wiggler field was developed at the European Synchrotron Radiation Facility (ESRF) (Serduc *et al.*, 2010). The same approach cannot be implemented at the Australian Synchrotron's Imaging and Medical Beamline (IMBL) due to existing constraints on the magnetic lattice of the storage ring, and therefore an alternative approach was developed. Our approach is based on the use of the double-crystal Laue monochromator at IMBL which produces two, spatially separated, beams. The first is the diffracted monochromatic beam, displaced by 20 mm from the primary transmitted beam. The intensity of the monochromatic beam can be greatly reduced, so can generate a low-dose beam for imaging. Switching between imaging and treatment is done by moving the relevant equipment from one beam to the other. The protocol is applicable for image guidance at the small-animal MRT station of the IMBL.

After describing the experimental setup, we discuss principles of operation of our protocol and how it is adapted for the opportunities and limitations of the IMBL source and geometry. Subsequently we discuss the imaging results, the dosimetry data and present the first proof-of-principle image-guided radiotherapy results. All data are discussed and critically analysed.

2. Materials and methods

Image guidance based on X-ray imaging is commonly available in clinical radiotherapy equipment. In modern systems, image guidance is performed with one or two independent kV X-ray sources and detectors. In the case of a single kV source, the source is mounted orthogonally to the plane of the treatment beam. Modern image guidance systems for stereotactic radiosurgery feature two kV sources which are positioned orthogonally with respect to one another and share the same isocenter as the treatment beam. The images acquired in this way can be readily matched to digitally reconstructed radiographs (DRRs) generated from a computed tomography (CT) scan used for treatment planning. The image registration and consequent patient positioning is performed in a semi-automated fashion prior to the treatment.

Developing an image-guidance protocol for synchrotron MRT should naturally follow the same philosophy, but

requires overcoming two notable problems: (i) the imaging beam and the treatment beam are not independent and (ii) the imaging technology available at synchrotron beamlines is markedly different from that available in clinics.

An imaging modality based on modification of the wiggler gap has been proposed at the ESRF (Serduc *et al.*, 2010). Increasing the wiggler gap, but keeping the other parameters the same, produces a low-intensity low-energy beam that can be used for imaging. This approach requires no modifications of the beamline parameters and the switch between imaging mode and therapy mode can be made in a relatively short time.

However, at the IMBL the wiggler field cannot be rapidly changed, as that would severely interfere with the normal storage ring operations of the Australian Synchrotron. We have therefore developed an alternative approach, as described in the following.

2.1. The MRT station at the IMBL

The IMBL source is a superconducting multi-pole wiggler (SCMPW), comprising 60 pole pairs (52 mm period) and operating at a peak magnetic field of 3.0 T. Relevant components for the image-guidance protocol are the in-vacuum filter vessel, located at 14.7 m from the source, and the double-crystal Laue monochromator (DCLM), whose center is at a distance of 16.15 m from the source [for more details about the beamline, see Stevenson *et al.* (2010, 2012) and Crosbie *et al.* (2013)]. The filter vessel contains five independent paddles, enabling different filtration options for the transmitted pink beam spectrum, that can be adapted for imaging or therapy applications.

The MRT station is located in Hutch 2B of the IMBL at a distance of approximately 34 m from the source. The station, shown in Fig. 1, is composed of a beam-defining aperture that sets the initial beam size of the broad beam (*i.e.* before the micro-planar beam production), a silicon detector, the micro-
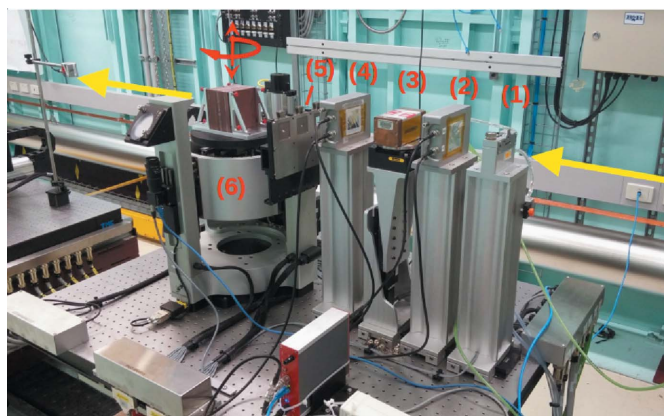

Figure 1
Photograph of the MRT station at IMBL. The beam propagation is from right to left (yellow arrows) and the main components are: (1) beam-defining aperture, (2) silicon beam monitor, (3) MRT collimator, (4) silicon beam monitor, (5) mask assembly (fixed to scanning stage), (6) sample scanning stage.

slit collimator for the microbeam production, followed by a second silicon detector. The sample stage, located after the second detector, allows for accurate scanning of the sample in the vertical direction as well as rotation about the vertical axis. The stage includes an assembly with three interchangeable mask positions that are used to define the effective illuminated area during scanning. The larger mask, typically used for imaging, has an area of 20 mm × 20 mm, while the other two masks, typically chosen in therapy mode, can be selected according to the area to be irradiated.

Downstream of the sample, at a variable distance between 2 and 3.5 m, a flat-panel X-ray detector (Hamamatsu C9259DK-14) is used for acquisition. The detector is used in partial scan mode, where the top 240 mm × 10 mm of the active area is read out, enabling a frame rate up to 146 frame s^{-1} with a pixel size of 100 µm. The detector features a CsI scintillator directly deposited onto the photo-diode array, to maximize the coupling efficiency of light with the photodiode array.

2.2. The concept of image guidance at IMBL

The silicon DCLM at IMBL produces a 20 mm vertical offset between the diffracted monochromatic beam and the transmitted pink beam. Once the monochromator is aligned, either beam can be selected by setting the appropriate beamline mode and moving all components to the relevant beam height, without further changes to the position of the crystals. This means there is no need to move the crystals out of the beam when the pink beam is selected, and the crystals (each approximately 1 mm thick along the beam direction) just act as additional filters. Therefore one can select the monochromatic beam for imaging and then, by translating the relevant beamline components and changing the beamline shutter mode, switch to pink beam for treatment.

Our image guidance protocol was developed following this principle: both imaging and treatment beam are available and can be selected by moving the relevant beamline components and switching between beamline operation modes, from monochromatic mode to MRT mode and *vice versa*. Taking advantage of the repeatability of motion stages and shutters of IMBL, by developing a custom script to perform the translation of all motion stages automatically, we can perform quick and accurate image-guided MRT at IMBL.

To achieve a seamless transition between imaging and therapy modes we had to find the optimal combination of beam filtering and monochromator settings to simultaneously have optimal spectrum for therapy and minimal dose for imaging. We chose the beam filtration featuring 0.45 mm graphene, 21.2 mm high-density graphite and 2.8 mm copper. Under these conditions, the pink beam spectrum at the sample position peaks at about 87 keV with a weighted average of 95 keV (see calculated spectrum in Fig. 2).

Imaging was performed at 50 keV, selected by the DCLM. The choice of the monochromatic energy was driven by imaging contrast, detector efficiency and dose considerations, and deserves some more explanation. Due to the limited beam
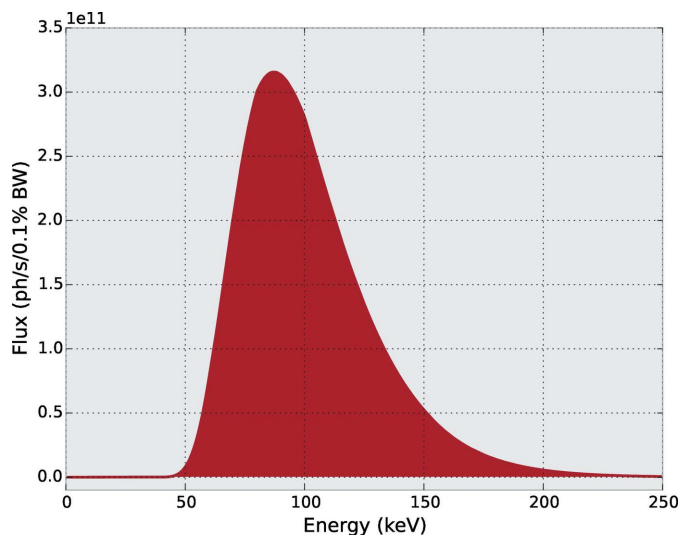

Figure 2
Calculated spectrum for a 20 mm (H) × 1 mm (V) beam size at the sample position (33.9 m from the source) in Hutch 2B at IMBL. Parameters used in the calculation are: 3.032 GeV storage ring energy, 200 mA storage ring current, SCMPW at 3.0 T peak magnetic field, emittance effects included. Filtering of the beam, as described in the text, has been included as well as additional windows, foils, air and He path present prior to the sample position.

size, an image of a sample is made by scanning the sample in the vertical direction as the detector is acquiring images. The image is then obtained by tiling individual sample views (more details can be found in the following section). Therefore, to minimize the imaging dose it is imperative that the sample vertical scan is performed as fast as possible. Denoting the scan speed by s and the exposure time by T, to avoid motion blur in the acquired image we require $sT < p$ where p is the pixel size of the detector. In our case we found a reasonable trade-off by setting the scan speed to 5 mm s^{-1} with an exposure time of 15 ms, resulting in $sT = 75$ µm, which is within the detector pixel size. At the same time, by scanning the sample with the 20 mm × 20 mm imaging mask the total scan time is a little over 4 s and the dose is kept to a minimum (see §4 and Appendix B). Having selected speed and exposure time, the energy had to be chosen to optimize both imaging contrast and counting statistics of the detector. For any monochromatic beam energy E, the DCLM also transmits the third harmonic at energy $3E$. The presence of the third harmonic degrades the imaging contrast. Therefore, if E is chosen too low, the third harmonic is predominant (note the asymmetric shape of the spectrum in Fig. 2), and the contrast is poor. Conversely, if E is too high, the first harmonic flux surges and this results in increased imaging dose and possible saturation of the detector.

The choice of 50 keV guarantees that the detector has optimal counting rate (about 75% of the flat-panel dynamic range in 15 ms exposure) and, at the same time, that the presence of the third harmonic at 150 keV is not entirely degrading the contrast. This point is not trivial since, for the chosen filtration, the number of photons of the third harmonic is about 19 times higher than the corresponding number of first harmonic photons (see Appendix A). The filtration is not

changed between therapy and imaging to avoid any change on the heat load of the monochromator. On the other hand, since the efficiency of the detector is much lower for the third harmonic, the detrimental effect of the high energy on the imaging contrast is reduced. Detailed considerations about the imaging contrast with the flat-panel detector can be found in Appendix *A*.

3. Imaging and sample alignment

3.1. Calibration procedures

Our proof-of-principle experiment comprised imaging and treatment of test samples from two orthogonal directions. We therefore devised a calibration procedure to ensure that the sample stays aligned in the treatment beam after a 90° rotation about a vertical axis. In practice that means ensuring that the sample feature to be irradiated is centered on the axis of rotation of the MRT stage.

Preliminary calibration is performed with an alignment pin, of the type typically used in goniometer heads, aligned in the beam and on the center of rotation of the MRT stage. The calibration procedure is as follows:

(i) Align the pin on the rotation axis of the MRT stage.

(ii) Move the tip of the pin to the height of the monochromatic beam.

(iii) Align two laser levels, parallel and perpendicular to the beam direction, to the tip of the alignment pin. The axis where the two laminar laser beams cross is approximately the rotation axis of the MRT stage. Once the laser cross has been calibrated, every sample can be optically aligned on the laser cross, before X-ray imaging.

3.2. Imaging and alignment procedure

Radiotherapy dose considerations inform the choice of the beam-defining aperture for the experiment. Three options are available at the IMBL MRT station: 0.5 mm, 1.0 mm and 2.0 mm vertical opening, with constant 30 mm horizontal opening. In any case (even in the absence of beam-defining apertures) the vertical beam size is too small to implement conventional full-field imaging and a scanning technique must be employed. An example of the beam shape at the detector is shown in Fig. 3.

Using a custom script written in Python, the sample stage is translated in the vertical direction at a speed of 5 mm s^{-1} while the detector is continuously acquiring images at a frame rate of 50 frames s^{-1} or faster. The script detects the center of
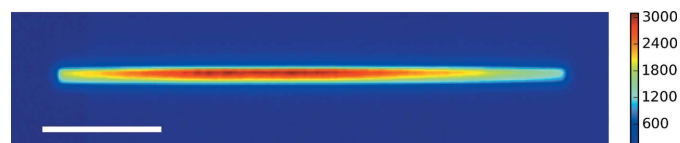
mass of the beam in the vertical direction, and extracts the row of pixels corresponding to that position. Then, the chosen row (or a rolling average of adjacent rows) is extracted from each image. The extracted rows are finally consecutively stacked (tiled) to reconstruct a full-field image of the sample.

The use of the 20 mm × 20 mm imaging mask, along with an edge detection algorithm that locates the mask edges, is used to constrain the aspect ratio of the reconstructed image, that would otherwise be dependent on the scan speed. The stacking procedure is performed in real time so that the operator can visualize the image of the sample shortly after the scan has been completed.

The images are visualized by the operator through an interactive graphical user interface (GUI). Screen shots of the GUI are shown in Fig. 4. The panel (*a*) shows the raw data acquired with the procedure just described. The 'sample'
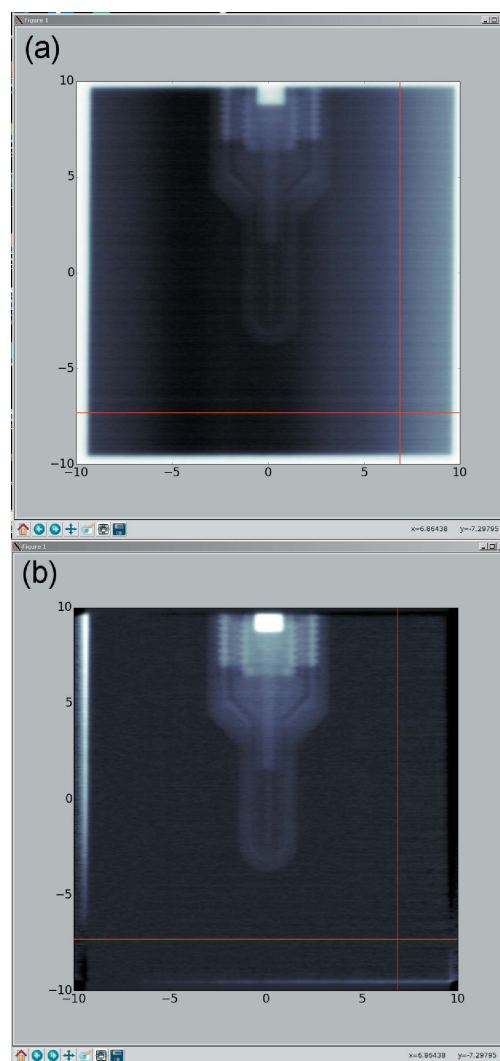

Figure 3
Image of the direct monochromatic beam at 50 keV onto the flat-panel detector, when a 20 mm (H) × 1 mm (V) beam-defining aperture is used. The scale bar corresponds to 5 mm and the color bar reports the number of counts in 15 ms exposure.

Figure 4
Screen shots of the tiled sample image, as visible to the operator after an imaging scan. (*a*) Raw image of a pinpoint ionization chamber. The image is limited by the 'imaging' mask of nominal size 20 mm × 20 mm. The crossed line cursor can be used to align the feature of interest at the center of the square mask (see text). (*b*) Flat-field corrected image of the same sample. In both images, white corresponds to stronger attenuation.
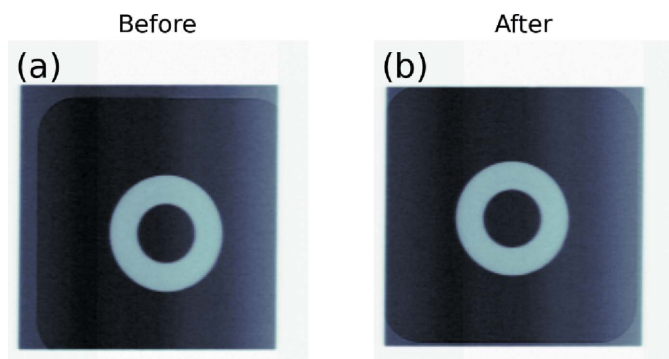
Daniele Pelliccia *et al.* · Image guidance protocol for synchrotron MRT

Figure 5
Image of a steel washer, (a) before the semi-automatic alignment and (b) after the alignment.

Figure 6
Normalized images of the live mice. (a) Tumor-bearing fifth mammary fat pad. (b) Leg without tumor. (c) Skull. (d) Portion of the spine. In all images the darker region corresponds to the window in the perspex holder.

imaged here is a pinpoint ionization chamber used for dosimetry (see below). To improve the visual contrast of the image a flat-field correction option can be selected, to normalize out the variations in the beam intensity profile. This is done using the very same scan, if a portion of open beam is acquired in the image. The flat-field corrected image for the pinpoint ionization chamber is shown in Fig. 4(b); visual contrast has improved and weak-contrast details of the sample (i.e. the tip of the ionization chamber) can be more readily distinguished.

The crossed lines visible in the GUI allow for semi-automatic sample alignment. In this case the operator needs only to click on the image feature to be aligned, and the script will drive the sample stages to have that feature at the center of the mask. An example is illustrated in Fig. 5 with an image of a steel washer. After optically aligning the washer with the laser cross, an image was taken as shown in Fig. 5(a). Using the interactive GUI, the operator can align the center of the washer at the center of the mask.

3.3. Live imaging

The procedure described above has been applied in a pilot experiment using tumor-bearing live mice. The tumors were inoculated into the right fifth mammary fat pad of the mice. The aim of the experiment was to study tumor response with varying radiation dose; however, selected mice were also imaged to test the capabilities of the system using live rodents.

The mice were sedated and fixed to a perspex holder. The holder had an opening corresponding to the site of the mammary fat-pad tumor. Hence the image of the region of interest was obtained without further attenuation or scattering from the perspex holder.

In addition to the tumor site, images were also taken of the left side fifth mammary fat pad that had not been inoculated with tumor cells, the skull and the spine. The images obtained are shown in Fig. 6, where the square darker region visible in all panels is the opening in the perspex holder. As can be appreciated, in this case there is no open beam region that can be used for flat-field correction. This can be a problem, especially if the beam displays significant intensity variations across its extent or the sample, as is the case for the mice, contains regions of very different attenuation. Nevertheless, also for this situation we can perform an image correction:
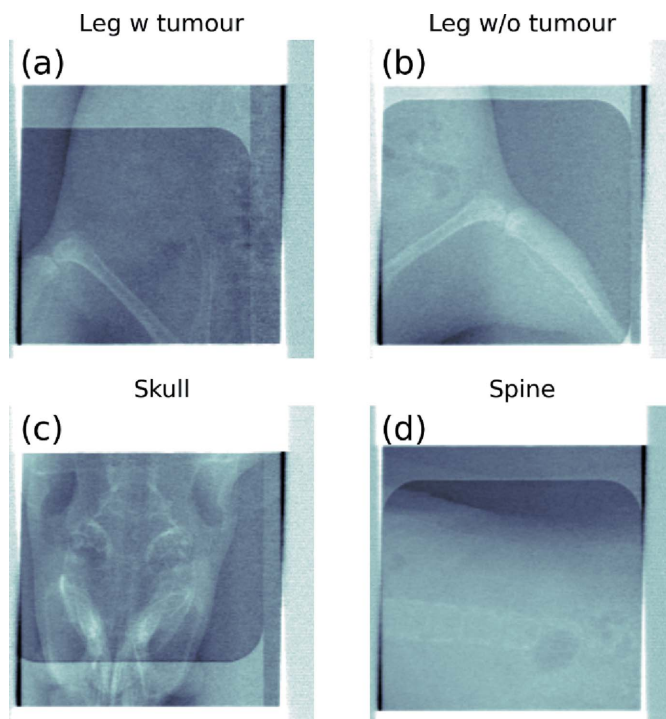
each row of the image is divided by the average of the image in the vertical direction. That is the way the images in Fig. 6 have been prepared. Strictly speaking, such a normalization is not quantitatively correct; nevertheless, the vertical average is quite effective in normalizing out the intensity variations in the beam (the sample features are averaged) and therefore the visual contrast is improved. This way of normalizing the images cannot be used for samples with strongly attenuated features, such as metals, as these features will skew the vertical average and therefore produce significant artefacts in the normalized images.

The quality of the images does not permit, at this stage, to gain information about the tumor position, shape or size, and therefore inform clinical decision making. Nonetheless, the bony anatomy can be clearly visualized, and this represents the first step towards patient positioning using bony landmarks. Accurate registration between monochromatic X-ray images taken at the synchrotron with external clinical imaging such as MRI depends on the accuracy of bony landmark localization (Bouchet et al., 2010; Serduc et al., 2010). Based on the results reported here, we plan to develop procedures for image registration between synchrotron and external sources such as MRI, including localization of the landmarks for subsequent precise positioning of target tumors using the synchrotron images.

3.4. Computed tomography

The availability of a rotating stage with high accuracy as a component of the MRT setup is an advantage when computed
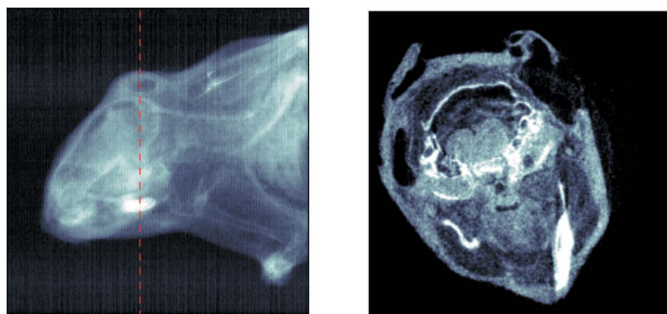
Figure 7
Left: radiography of a plastinated mouse head, acquired at the MRT station. The image as shown has been rotated by 90° with respect to the original position. Right: CT slice, acquired in real time, of the same sample at the position marked by the red dashed line in the left-hand image.

Figure 8
Measured air kerma as a function of the scan speed. See Appendix B for details.

tomography (CT) is required. The limited vertical dimensions of the beam, along with the presence of the beam-defining aperture, only permits up to a 2 mm vertical distance on the sample to be illuminated, and therefore only a few CT slices can be acquired in one measurement. However, a 180° CT scan can be acquired in a few seconds using the same imaging procedure, this time with the rotating stage in place of the translation stage. In this experiment we set the rotation scan speed to 15° s^{-1}, but the stage can rotate more rapidly if required.

In this way a real-time CT scan can be recorded, if required, in a region of interest of the sample, once it has been aligned at the center of the beam. An example is shown in Fig. 7. In the left panel is an attenuation image of a plasticized heterogeneous mouse specimen (plastinated mouse) (van Hoof *et al.*, 2013). The red dashed line marks the position where the sample has been aligned for the CT scan. The reconstructed slice is shown in the right-hand panel of Fig. 7.

4. Dosimetry

Following the approach used in the code of practice for dosimetry in radiology (Alm-Carlsson, 2007), we measured air kerma and derived the absorbed dose to water rates. We have performed the measurements in imaging mode, to verify that the imaging procedure can be performed with low dose. Note that 'imaging mode' means using a monochromatic beam without the micro-slit collimator. Dosimetry was performed using a PTW pinpoint ionization chamber (model TN31014), which was recently calibrated for air kerma at various kV beam qualities at Physikalisch-Technische Bundesanstalt (PTB), Germany.

Owing to the very low dose rate in imaging mode, we measured the charge accumulated on the pinpoint ionization chamber, scanning the vertical stage at different speeds. For each speed we repeated the measurement three times and averaged the result. Then, following Klevenhagen *et al.* (1996) and the procedure described in Appendix B, we derived air kerma and dose rate at the sample surface. Air kerma results are displayed in Fig. 8, showing air kerma as a function of the
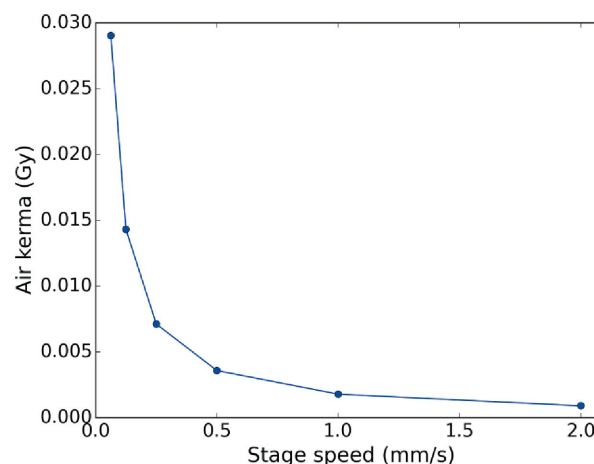
scan speed. As expected, the rate is constant, the measured values are 1.79 ± 0.01 mGy s^{-1} for the air kerma rate and 1.96 ± 0.01 mGy s^{-1} for the dose rate at the sample surface.

5. Proof of concept of image-guided radiotherapy

To verify the spatial accuracy of the therapy beam on the target, we employed radiochromic 3D PRESAGE® dosimeters. PRESAGE (Guo *et al.*, 2005) is a solid, transparent dosimeter based on polyurethane. Radiation exposure causes a radiochromic color change in the dosimeter.

A dosimeter was cast in the approximate shape of a cylinder and subsequently a circular hole was drilled in it to host a ball bearing with a diameter of 3/16 inch (~4.76 mm). Rather than using it for dosimetry, we used PRESAGE to track the microplanar beam tracks along the cylinder and the spatial accuracy of the beam tracks with respect to the ball bearing.

Images of the ball bearing at two different orientations are shown in Fig. 9. We imaged the sample at a scanning speed of 5 mm s^{-1} with the 20 mm × 20 mm imaging mask at both 0° and 90° orientation [Figs. 9(a) and 9(b), respectively]. We aligned the ball at the center of the mask for both orientations, then switched to a circular mask with 5 mm diameter and imaged the sample with the new mask, again in both orientations [Figs. 9(c) and 9(d), respectively].

As the ball bearing is slightly smaller than the circular mask, it is easy to visualize the accuracy of the alignment. Results are displayed in Fig. 9. The accuracy of the alignment is approximately 100 µm, corresponding to the effective pixel size of the flat-panel detector.

Having established an imaging protocol, we subsequently demonstrated the proof-of-concept radiotherapy using two-beam irradiation. The complete image-guided radiotherapy was completed using the following procedure:

(i) Optically align the sample using the position of the laser cross, approximately corresponding to the rotation axis of the MRT stage.

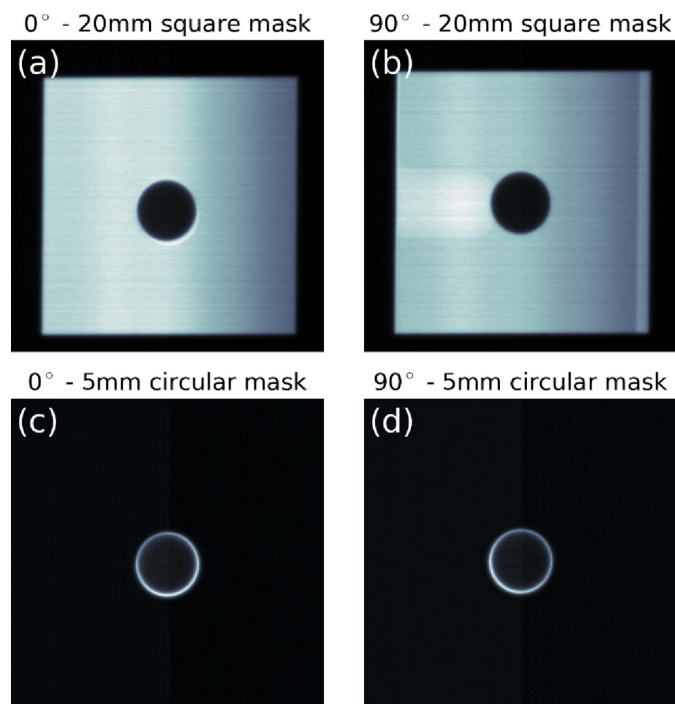(ii) Perform the Search & Secure procedure to lock the experimental hutch and allow opening of the shutter.

Figure 9
(*a*) Image of the ball bearing in the PRESAGE phantom at 0° nominal orientation through the 20 mm × 20 mm mask. (*b*) Corresponding image at 90° orientation. (*c*) Image through the 5 mm-diameter circular mask at 0° nominal orientation. (*d*) Corresponding image at 90° orientation.

(iii) With the beamline in monochromatic beam mode, take an image of the sample at 0° orientation and align the sample at the center of the 20 mm × 20 mm mask. No micro-slit collimator is in the beam during the imaging procedure.

(iv) Take an image of the sample at 90° orientation and align the sample at the center of the mask.

(v) Switch the beamline configuration to MRT Mode and automatically realign all relevant beamline components, including inserting the micro-slit collimator, setting the appropriate mask in place of the imaging mask, and moving the detector out of the beam to prevent damage.

(vi) Perform the treatment of the sample, scanning the vertical MRT stage at the desired speed, according to the dose to be delivered. The treatment is performed at 0° and 90° consecutively. If required, the mask can be changed between the two treatments.

The result of the treatment on the PRESAGE phantom is shown in Fig. 10, where panel (*a*) shows a schematic of the irradiation geometry and panel (*b*) shows a photograph of the beam tracks around the ball bearing. The micro-planar beam geometry is clearly visible in one of the two beams; see also the close-up photograph in panel (*c*).

The whole procedure, *i.e.* two orthogonal images, alignment and verification, beamline mode change and two treatments at orthogonal positions, has been completed in under 6 min. The relatively short duration (which can be decreased if only a single imaging or irradiation is required) makes our protocol compatible with synchrotron MRT of sedated small animals.
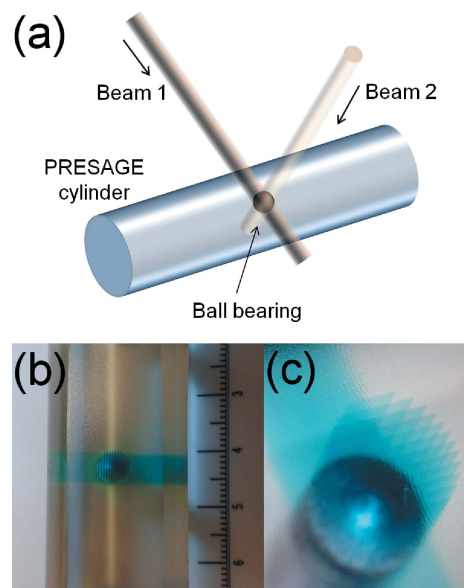

Figure 10
Irradiation of the radiochromic PRESAGE dosimeter with embedded ball bearing. (*a*) Schematic of the beam irradiation geometry. (*b*) Photograph of the micro-planar beam tracks (green) in orthogonal directions over the ball bearing to testify the spatial accuracy of the therapy procedure. (*c*) Close-up photograph of the region around the ball bearing.

6. Conclusions

In conclusion, we have shown an image guidance protocol for synchrotron MRT. The protocol has been implemented at the Imaging and Medical Beamline at the Australian Synchrotron, with a dedicated stage for MRT.

The image guidance is based on the use of the double-crystal Laue monochromator at IMBL which produces two, spatially separated, beams. The intensity of the monochromatic beam is greatly reduced, to generate a low-dose beam for imaging. Switching between imaging and treatment is done by moving the relevant equipment from one beam to the other.

We have demonstrated that the imaging and treatment procedure can be performed with an accuracy of about 100 µm, corresponding to the effective pixel size of the detector. The accuracy of the therapy has been verified with a radiochromic 3D PRESAGE® dosimeter able to store the microbeam tracks in 3D.

The procedure we demonstrated is capable of high-accuracy rapid synchrotron MRT optimized for small animals. The working principle is currently being extended to MRT for larger animals.

APPENDIX *A*
Imaging contrast considerations

With reference to Fig. 2, the spectral photon flux [photons s^{-1} (0.1% bandwidth)$^{-1}$] is $N_1 = 0.81 \times 10^{10}$ at 50 keV and $N_3 = 5.2 \times 10^{10}$ at 150 keV. In addition, considering that the transmitted bandwidth is three times larger at 150 keV

compared with at 50 keV (Erola *et al.*, 1990), we have a ratio $R = 3N_3/N_1 \simeq 19$ between the number of photons at 150 keV and the number of photons at 50 keV. Nevertheless, the different conversion efficiency of the CsI scintillator (that is more efficient at 50 keV) results in a ratio between visible-light photons of

$$r = R \frac{1 - \exp(-\mu_3 t)}{1 - \exp(-\mu_1 t)} \approx 0.84, \tag{1}$$

where $t = 150\ \mu m$ is the scintillator thickness (estimated value), and $\mu_1 \simeq 1.27\ mm^{-1}$ and $\mu_3 \simeq 0.07\ mm^{-1}$ are the linear attenuation coefficients of the CsI scintillator for the first and third harmonic, respectively.

APPENDIX *B*
Considerations for the dosimetry in imaging mode

The absorbed dose at the sample surface can be calculated with the approached described by Klevenhagen *et al.* (1996) for low-energy X-rays:

$$D = MN_K K_{tp} B_w \left[(\bar{\mu}_{en}/\rho)_{w/a} \right]_a. \tag{2}$$

D is the dose to water surface in Gy, M is the ion chamber reading, N_K is the chamber calibration factor, K_{tp} is the temperature–pressure–humidity correction factor, B_w is the back-scatter factor and $[(\bar{\mu}_{en}/\rho)_{w/a}]_a$ is the mass energy absorption coefficient (MEAC) ratio water-to-air averaged over the X-ray spectrum in air.

The formula above is valid for polychromatic X-rays. To calculate the air kerma and the surface dose in our image guidance experiment, we must consider an alternative formula based on monochromatic X-rays. In fact, we should consider that we have a spectrum made of two lines: the first and the third harmonic. The formula must therefore be modified as follows:

$$\begin{aligned} D = MK_{tp} \Big\{ &\alpha N_K^{(1)} B_w^{(1)} \left[\left(\mu_{en}^{(1)}/\rho \right)_{w/a} \right]_a \\ &+ \beta N_K^{(3)} B_w^{(3)} \left[\left(\mu_{en}^{(3)}/\rho \right)_{w/a} \right]_a \Big\}. \end{aligned} \tag{3}$$

Here, the superscripts (1) and (3) refer to the first and third harmonics, respectively. The constants α and β are obtained by the ratio of the intensities between the first and third harmonic, $\alpha/\beta \simeq 0.052$ (see Appendix *A* and the spectrum in Fig. 2), and the factors $N_K^{(1)} \simeq 2.17 \times 10^9\ Gy\ C^{-1}$ and $N_K^{(3)} \simeq 2.09 \times 10^9\ Gy\ C^{-1}$ are the calibration factors obtained by PTB.

References

Alm-Carlsson, G. (2007). *Dosimetry in Diagnostic Radiology: An International Code of Practice.* International Atomic Energy Agency Technical Reports Series No. 457.

Bouchet, A., Lemasson, B., Le Duc, G., Maisin, C., Bräuer-Krisch, E., Siegbahn, E. A., Renaud, L., Khalil, E., Rémy, C., Poillot, C., Bravin, A., Laissue, J. A. & Serduc, R. (2010). *Int. J. Radiat. Oncol. Biol. Phys.* **78**, 1503–1512.

Bräuer-Krisch, E., Serduc, R., Siegbahn, E., Le Duc, G., Prezado, Y., Bravin, A., Blattmann, H. & Laissue, J. (2010). *Mutat. Res. Rev. Mutat. Res.* **704**, 160–166.

Crosbie, J. C., Anderson, R. L., Rothkamm, K., Restall, C. M., Cann, L., Ruwanpura, S., Meachem, S., Yagi, N., Svalbe, I., Lewis, R. A., Williams, B. R. G. & Rogers, P. A. W. (2010). *Int. J. Radiat. Oncol. Biol. Phys.* **77**, 886–894.

Crosbie, J. C., Rogers, P. A., Stevenson, A. W., Hall, C. J., Lye, J. E., Nordström, T., Midgley, S. M. & Lewis, R. A. (2013). *Med. Phys.* **40**, 062103.

Dilmanian, F. A., Button, T. M., Le Duc, G., Zhong, N., Pena, L. A., Smith, J. A., Martinez, S. R., Bacarian, T., Tammam, J., Ren, B., Farmer, P. M., Kalef-Ezra, J., Micca, P. L., Nawrocky, M. M., Niederer, J. A., Recksiek, F. P., Fuchs, A. & Rosen, E. M. (2002). *Neuro Oncol.* **4**, 26–38.

Erola, E., Eteläniemi, V., Suortti, P., Pattison, P. & Thomlinson, W. (1990). *J. Appl. Cryst.* **23**, 35–42.

Grotzer, M., Schültke, E., Bräuer-Krisch, E. & Laissue, J. A. (2015). *Phys. Med.* **31**, 564–567.

Guo, P., Adamovics, J. & Oldham, M. (2005). *Int. J. Radiat. Oncol. Biol. Phys.* **63**, S206.

Hoof, S. J. van, Granton, P. V. & Verhaegen, F. (2013). *Radiother. Oncol.* **109**, 361–366.

Klevenhagen, S. C., Aukett, R., Harrison, R., Moretti, C., Nahum, A. & Rosser, K. (1996). *Phys. Med. Biol.* **41**, 2605–2625.

Laissue, J. A., Geiser, G., Spanne, P. O., Dilmanian, F. A., Gebbers, J.-O., Geiser, M., Wu, X.-Y., Makar, M. S., Micca, P. L., Nawrocky, M. M., Joel, D. D. & Slatkin, D. N. (1998). *Int. J. Cancer*, **78**, 654–660.

Laissue, J. A., Lyubimova, N., Wagner, H.-P., Archer, D. W., Slatkin, D. N., Di Michiel, M., Nemoz, C., Renier, M., Brauer, E., Spanne, P. O., Gebbers, J.-O., Dixon, K. & Blattmann, H. (1999). *Proc. SPIE*, **3770**, 38–45.

Serduc, R., Berruyer, G., Brochard, T., Renier, M. & Nemoz, C. (2010). *J. Synchrotron Rad.* **17**, 325–331.

Slatkin, D., Spanne, P., Dilmanian, F., Gebbers, J. & Laissue, J. (1995). *Proc. Natl Acad. Sci. USA*, **92**, 8783–8787.

Slatkin, D. N., Spanne, P., Dilmanian, F. A. & Sandborg, M. (1992). *Med. Phys.* **19**, 1395–1400.

Stevenson, A. W., Hall, C. J., Mayo, S. C., Häusermann, D., Maksimenko, A., Gureyev, T. E., Nesterets, Y. I., Wilkins, S. W. & Lewis, R. A. (2012). *J. Synchrotron Rad.* **19**, 728–750.

Stevenson, A. W., Mayo, S. C., Häusermann, D., Maksimenko, A., Garrett, R. F., Hall, C. J., Wilkins, S. W., Lewis, R. A. & Myers, D. E. (2010). *J. Synchrotron Rad.* **17**, 75–80.

Timmerman, R. D. & Xing, L. (2012). *Image-Guided and Adaptive Radiation Therapy.* Baltimore: Lippincott Williams & Wilkins.